Lidar depolarization characterization using a reference system

Alkistis Papetta[1], Franco Marenco[1], Maria Kezoudi[1], Rodanthi-Elisavet Mamouri[2,3], Argyro Nisantzi[2,3], Holger Baars[4], Ioana Elisabeta Popovici[5,6], Philippe Goloub[6], Stéphane Victori[5], and Jean Sciare[1]

[1]The Cyprus Institute, Nicosia, Cyprus
[2]Cyprus University of Technology, Limassol, Cyprus
[3]ERATOSTHENES Centre of Excellence, Limassol, Cyprus
[4]Leibniz Institute for Tropospheric Research, Leipzig, Germany
[5]Cimel Electronique, Paris, France
[6]University of Lille, CNRS, LOA - Laboratoire d'Optique Atmosphérique, Lille, France

Correspondence: Alkistis Papetta (a.papetta@cyi.ac.cy)

Abstract. In this study, we will present a new approach for the determination of polarization parameters of the Nicosia CIMEL CE376 lidar system, using the Polly^{XT} in Limassol as a reference instrument. The method is applied retrospectively to the measurements obtained during the 2021 Cyprus Fall campaign. Lidar depolarization measurements represent valuable information for aerosol typing and for the quantification of some specific aerosol types such as dust and volcanic ash. An accurate
5 characterization is required for quality measurements and to remove instrumental artefacts. In this article, we use the Polly^{XT}, a widely used depolarization lidar, as our reference to evaluate the CE376 system's gain ratio and channel cross-talk. We use observations of transported dust from desert regions for this approach, with layers in the free troposphere. Above the boundary layer and the highest terrain elevation of the region, we can expect that for long transport aerosols local effects should not affect the aerosol mixture so that we can expect similar depolarization properties at the two stations (separated by ~60 km).
10 Algebraic equations are used to derive polarization parameters from the comparison of the volume depolarization ratio measured by the two systems. The applied methodology offers a promising opportunity to evaluate the polarization parameters of a lidar system, in cases where a priori knowledge of the cross-talk parameters is not available, or to transfer the polarization parameters from one system to the other.

1 Introduction

15 Understanding the aerosol vertical stratification can help in reducing the uncertainties related to aerosol radiative forcings which remain large (IPCC , 2021). For more accurate estimations, it is essential to improve the knowledge of the aerosol characteristics: shape, size and optical properties. The diversity of combinations of aerosol sources and transport mechanisms leads to the high variability of the distribution of aerosols with different characteristics, which makes their classification a complicated task (Di Iorio et al., 2003).

20   Lidar has become a widely used tool for studying highly resolved information on the spatial and temporal distribution of aerosols. On this, several key campaigns, such as SAMUM 1, 2 (Groß et al., 2011; Tesche et al., 2011) and the ASKOS experiment (Marinou et al., 2023), were performed and successfully demonstrate the capabilities of lidar systems. These were

not the first to demonstrate aerosol lidars, e.g., Reagan et al. (1977); Brogniez et al. (1992); Krueger (1993). In contrast to traditional set-ups with in situ or airborne sensors, like optical particle counters (OPC) or particle sizers (Di Girolamo et al., 2022), lidars (ground or satellite-based) can provide information on the temporal variability and on the vertical structure up to the stratosphere. In addition, it provides insights on aerosol size and optical properties.

Cyprus, situated between large deserts, is actively involved in advancing atmospheric science and aerosol research. The region's unique location has made it an invaluable site for diverse studies on dust and not only (e.g., detection of Canadian wildfire smoke over Cyprus, Baars et al.2019). For example Mamouri and Nisantzi's work (2013; 2014; 2016; 2016b; 2014; 2015) introduced novel methodologies for dust profiling using polarization lidar, analyzing dust outbreaks over Cyprus. Nisantzi et al. (2014, 2015) explored lofted fire smoke plumes' mineral dust content and compared extinction ratios for desert dust in Cyprus. Mamouri et al. (2016) comprehensively detailed extreme dust storms in the Cyprus region, showcasing EARLINET lidar observations. Additionally, studies by Kezoudi et al. (2021) and Mamali et al. (2018) compared UAV-based OPC observations with lidar, enriching knowledge on Saharan dust over Cyprus. Moreover, key campaigns CyCARE/ALIFE had strong contributions by depolarization lidar and aimed to investigate properties of complex aerosol mixtures often observed over the island of Cyprus (Ansmann et al., 2019; Floutsi et al., 2023). These collective efforts highlight Cyprus's significant contributions to the understanding of aerosol properties.

The contribution of lidar to greater science is undoubtedly important as it is a fundamental tool for monitoring anthropogenic and natural aerosols. Sand and dust storms, or volcanic ash transport in case of volcanic eruptions, can impact human health and everyday life. WMO Sand and Dust Storm Warning Advisory and Assessment System (SDS-WAS), benefits from available lidar networks (e.g., EARLINET, Bösenberg , 2003) for the monitoring of vertical profiles of winds and aerosols (Basart et al., 2019). Similarly, lidars installed across different locations aim to improve detection and aid forecasting of volcanic ash in the event of future eruptions, by providing observations to local Volcanic Ash Advisory Centres (VAAC) (Sassen et al., 2007; Osborne et al., 2022a).

The addition of a depolarization channel on a lidar system offers the capability to discriminate between different types of atmospheric particles, for example, low depolarizing urban aerosols and high depolarizing dust aerosols, or liquid and ice clouds. Discriminating between liquid and ice water can provide a better understanding of the aerosol-cloud interactions (e.g., Seifert et al. 2010). Aerosols can change the properties of clouds and therefore affecting indirectly their radiative forcing (Senior and Mitchell, 1993; Fowler and Randall, 2002). Aerosol typing can be quite complex when the observed atmospheric layers consist of multiple aerosol types.

Lidar depolarization measurements represent an excellent method to detect and quantify some specific aerosol types such as dust and volcanic ash (Cairo et al., 1999; Tesche et al., 2009; Freudenthaler et al., 2009). Using this information, several studies aim to describe the properties and temporal evolution of each of the aerosol layers types (Hoffmann et al., 2010; Ansmann et al., 2011; Marenco and Hogan, 2011). They also permit the distinction between ice crystals and water droplets (Ansmann et al., 2005) and to discriminate the type of polar stratospheric clouds (Toon et al., 2000). The depolarization lidar technique is simple and reliable and is not as limited by daylight background as in the case of acquiring Raman signals.

Spherical particles in the atmosphere have no depolarization for 180° backscattering (Van de Hulst , 1957), hence a depolarization signal is an indication of non-sphericity such as in ice crystals or irregularly shaped aerosols. Most lidar systems use linearly polarized lasers (linear depolarization measurements), and such systems are used also in this paper. Some circular polarization lidar systems exist, such as eVe (Enhancement and Validation of ESA products), which provide useful information for layers with oriented particles and where multiple scattering cannot be neglected (Paschou et al., 2022).

Volume linear depolarization ratio (VLDR) or simply volume depolarization ratio (VDR) is usually defined as the ratio between the atmospheric cross sections for cross-polarized and co-polarized backscattering, and is a measure of the overall properties of the atmospheric volume, comprising a mixture of molecules and particles. This is typically measured by means of a polarizing beamsplitter in the receiving system, and taking the ratio of signals in the two channels. In reality, the measurement is more complex than this, and it requires to account for the gain ratio of the channels and for the cross-talk between them: this is what here we refer to as the determination of the lidar polarization parameters. If this step is not achieved correctly, systematic errors appear with a significant impact.

Addressing instrumental effects on depolarization channels is pivotal as numerous optical components within lidar systems can introduce substantial systematic errors in atmospheric depolarization values. Freudenthaler et al. (2016) introduced analytical equations to assess the dependence of lidar signals on polarisation parameters and different calibration setups. Both Bravo-Aranda et al. (2016); Belegante et al. (2018) emphasize that systematic errors can be significant if the lidar system is not well characterized and aligned, underscoring the need for careful consideration of optical components. Well-characterized VDR measurements permit on the one hand reconstruction of the total lidar signal, by the recombination of the two channels: this is needed for the retrieval of the particle backscattering and extinction coefficients. On the other hand, they permit the computation of the particle linear depolarization ratio (PLDR) or simply particle depolarization ratio (PDR), which abstracts from the influence of air molecules and is hence an intrinsic property of the particles (Freudenthaler et al., 2009). In a well characterised lidar system for depolarization, the channel gain ratio and all the elements contributing to an imperfect separation of the depolarization channels in the hardware are well known. The latter include the polarizing beam splitter transmittances and reflectances for the co-polar and cross-polar beams, as well as the laser polarization purity and its rotation angle compared to the frame of reference of the receiver (Freudenthaler et al., 2009, 2016). In particular, the laser rotation angle ϕ is not easily known, and an additional experimental apparatus has been used in a few papers in order to quantify it (Alvarez et al., 2006; Belegante et al., 2018; Osborne , 2022b). The additional apparatus consists of a rotatable half-wave plate added in front of the receiver optical path, and a calibration sequence has to be performed where atmospheric measurements are acquired by artificially varying the system's cross-talk through the rotation of the half-wave plate.

At the Cyprus Institute, we have recently acquired a new compact CIMEL CE376 lidar system, which we have operated continuously in Nicosia, Cyprus, since September 2021. This is a low-power and compact two-wavelength lidar system, ideal for campaigns and mobile observations, able to operate in all weather conditions, and able to detect the molecular signal up to 10 km in the daytime and 18 km in the nighttime with a good signal-to-noise ratio. We have however found an issue in the initial depolarization calibration, related to the observed VDR of purely molecular layers which is too high compared to the expected value computed according to Behrendt and Nakamura (2002). Whereas a technological solution is planned with CIMEL in the

near future, this paper is about a method for correcting past data, by correlating the lidar measurements to a reference calibrated lidar system, also located on the island, which for this paper we consider to be our reference system. This will be called the atmospheric characterization approach to the lidar polarization parameters.

95   In Section 2, we present the depolarization lidar equations to be used for the depolarization characterization. Following in Section 3, we describe the systems used in this study, focusing on the technical characteristics and locations. Section 4, presents the lidar depolarization characterization methodology providing demonstration examples from past observations. Finally, Section 5, summarizes and concludes the main findings of the application of the discussed method.

2   Theoretical concept

100   In an ideal depolarization lidar, the range-corrected signal in the co-polar and cross-polar channels, $P^{||}$ and $P^{\perp}$, can be expressed as follows, in the function of the atmospheric volume cross sections $\beta^{||}$ and $\beta^{\perp}$ for non-depolarizing and depolarizing backscattering, respectively:

$$P^{||}(R) = K^{||}\, T(R)\, \beta^{||}(R) \tag{1}$$

$$P^{\perp}(R) = K^{\perp}\, T(R)\, \beta^{\perp}(R), \tag{2}$$

105   where R is the range, $T(R)$ is the two way atmospheric transmittance between ranges 0 and R, and $K^{||}$, $K^{\perp}$ are the lidar constants for both channels.

     The VDR is defined as the ratio $\delta = \beta^{\perp}/\beta^{||}$. Note that cross-polarizing backscatter $\beta^{\perp}$ is unphysical and that other definitions of VDR exist in the literature (see Gimmestad, 2008; Freudenthaler et al., 2016). However, the one used here has been commonly used in the legacy lidar literature (e.g. Freudenthaler et al., 2009). In the ideal case, VDR is computed as:

110
$$\delta = \frac{\delta^*}{K^*}, \tag{3}$$

     where $\delta^* = P^{\perp}/P^{||}$ is the ratio of the two lidar signals (a sort of uncalibrated depolarization ratio), and $K^* = K^{\perp}/K^{||}$ is the gain ratio between the two channels. For an ideal lidar, determining K^* is all that is needed to calibrate depolarization. Once this is done, then the lidar range-corrected total signal, P, can be reconstructed as a signal proportional to $\beta^{||} + \beta^{\perp}$. Hence:

115
$$P = P^{||} + \frac{P^{\perp}}{K^*}. \tag{4}$$

     $P(R)$ is what will be used in aerosol inversion schemes such as Fernald-Klett (Klett 1985, Fernald 1984) or Raman inversion (Ansmann et al., 1990, 1992a, b; Ferrare et al., 1998).

For a real depolarisation lidar system, the equations need to account for the cross-talk between the two channels, through the cross-talk constants, denoted as g and e in this paper, expressing respectively how much co-polar signal enters the cross-polar channel and vice versa, leading to the following expressions:

$$P^{||} = K^{||}\, T\, (\beta^{||} + e\,\beta^{\perp})$$
(5)

$$P^{\perp} = K^{\perp}\, T\, (\beta^{\perp} + g\,\beta^{||})$$
(6)

By dividing Eqs.6 and 5 we derive δ^*:

$$\delta^* = K^* \frac{\delta + g}{1 + e\delta} \quad,$$
(7)

which can be resolved as follows:

$$\delta = \frac{\delta^* - K^*\, g}{K^* - e\,\delta^*} \quad,$$
(8)

and the total signal can be then calculated by:

$$P = (1 - g)\, P^{||} + (1 - e)\, \frac{P^{\perp}}{K^*} \quad.$$
(9)

These full equations are going to be applied for the determination of the polarization parameters. In Freudenthaler et al. (2009, 2016), the approach is that we know our system well enough including the various parameters contributing to errors in depolarization calibration so that calibration only involves determining K^*. In our case, we assume we don't know our system to this point, and we will retrieve these parameters from observations and a reference system (we call this the three-parameter depolarization characterization, since K^*, g and e are to be retrieved).

The effect of g will usually dominate in low depolarization layers (e.g., particle free or spherical particle layers), so that we can attempt at simplifying Eq. 8 by neglecting e:

$$\delta = \frac{\delta^*}{K^*} - g,$$
(10)

which can be summarised in a phrase by saying that, in addition to knowing the gain ratio K^*, we must also know the "depolarization of the lidar system", g (more precisely diattenuation), or alternatively that depolarization equation involves a multiplicative and an additive parameter. Whereas it may not be the most correct way to neglect e for all lidar systems, this

140 simplified equation has been used in the past for some systems: for example, it was used in Marenco and Hogan (2011), Eq. (5) and in Chazette et al. (2012), Eq. (6). We call the approach using this simplified equation the two-parameter depolarization characterization (given that only K^* and g can be determined). It must be noted that in high depolarizing layers, the contribution of e is larger and therefore it should not be neglected (unless $e << 1$ for a particular system).

The following sections investigate these approaches and will highlight their advantages and drawbacks, and compare their
145 outcomes.

3 Instruments

3.1 CIMEL Lidar system

As it was briefly introduced before, CIMEL CE376 is a compact elastic backscatter lidar developed by CIMEL in France (seen in Fig. 1a). It is a dual-wavelength polarization lidar equipped with a laser diode and a frequency doubled Nd:YAG laser,
150 operating in the near infrared (808 nm) and green (532 nm) with a repetition rate of 4.7 kHz. It has a small beam divergence (50 µrad) and field-of-view (120 µrad) making it suitable for aerosol profiling. It measures backscatter signals in three reception channels, one for the infrared and two for green, co-polar and cross-polar channels. The lidar uses photon counting acquisition through avalanche photodiode detectors (SPCM-AQRH modules from Excelitas), for all the reception channels (schematic in Appendix E). The system has day and night operation with a typical detection altitude of around 10 km for the day and 18 km
155 for the night. The signal is recorded in 2048 successive bins spaced by 15 m in the vertical direction from 100 m up to a range of 30 km. The integration time is 1s. Before the raw CIMEL lidar data can be used for the depolarization characterization method, it must be pre-processed to correct detection errors and remove ambient background signals on all three channels. The pre-processing that we apply is dead time, dark count and background correction of the raw CIMEL data. Furthermore, data are filtered for quality assurance based on applied thresholds on housekeeping parameters (relative humidity and temperature).
160 The CIMEL lidar was installed in September 2021 at the Cyprus Institute premises in Nicosia, Cyprus [N35°8′29.23″, E33°22′51.49″] at 181 m above sea level (asl) and has been running continuously since. It was installed with a mechanical orientation directly to the vertical, ensuring vertical beam propagation with a precision of 1-2 µrad.

Nicosia is located in the center of the island, between the largest mountain ranges of Cyprus: Troodos stretching across a third of the island peaking at 1952 m and Kyrenia mountain range that runs along the northern coast of the island peaking at 1024 m
165 (see Fig. 2). The aerosol mixture above Nicosia is often a mixture between dust particles and anthropogenic haze.

The depolarization calibration suggested by the manufacturer follows the $\Delta(\pm 45°)$ method described in Freudenthaler et al. (2009), later renamed to $\Delta(90°)$ (Freudenthaler et al., 2016). To rotate the plane of polarization a half-wave plate (HWP) is used in front of the polarizing beamsplitter cube. Note that a priori knowledge of the cross-talk parameters is required for this method, therefore, we use transmittances (T_p, T_s) provided by the polarizing beam splitter (PBS) manufacturer (shown in
170 Table 1) for the calibration constant (V* in Freudenthaler et al. (2009), Eq.10) calculations.

A depolarization calibration was performed during the installation of the lidar in order to derive the calibration coefficient V^*, for the depolarization channel at 532 nm (found to be $V^* = 1.17$. $V^* \simeq K^*$, see Appendix A to understand the exact

(a)   (b)

Figure 1. CE376 lidar with thermal enclosure on Cyprus Institute premises roof in Nicosia (a) and Polly^{XT} container housing in CUT premises in Limassol (b).

	Tp (%)	**Ts (%)**	**V***
Period 1 (21/09/2021-05/01/2022)	1.03	99.92	1.17
Period 2 (11/01/2022-now)	0.45	99.8	0.78

Table 1. Characteristic $\Delta(90°)$ PBS calibration coefficient (V*) and transmittances for the parallel and perpedicular polarizations (T_p and T_s).

relationship between V^* and K^*). However, the molecular depolarization at 5–5.5 km was measured to be ∼40 times larger than the computed molecular depolarization for the lidar characteristics. According to Behrendt and Nakamura (2002), for a narrow filter of 0.2 nm, which corresponds to the narrow filter of CIMEL CE376, the computed molecular VDR is $\delta_m = 0.0036$. As this issue seemed to originate from the instrument and not the calibration, on January 2022, CIMEL intervened on site on the instrument to replace the PBS with a new one and repeated the calibration (giving a new $V^* = 0.78$). The PBS replacement did not suffice to improve the polarization measurements issue, which could be due to optical components inside the receiver and/or residual polarization from the laser. The intervention marks the conclusion of our first defined period and serves as the beginning of the second period defined as period 1 and 2 (dates seen on Table 1). Fig. 3, summarizes these findings by comparing the computed molecular depolarization (δ_m) to two observed profiles on aerosol free days from periods 1 and 2.

There are technical solutions that can be followed in order to improve the characterization of the system. Adding a motorized half-wave plate can reduce the human induced uncertainty during the calibration procedure, but this wouldn't resolve the cross-talk issue. Moreover, wire grid polarizers can be added on the PBS to reduce the cross-talk. The latter is planned

185 for the near future, but wouldn't help to correct the depolarization measurements that were acquired so far. Such valuable measurements were obtained for more than one year in Nicosia, including the Fall campaign that was performed in Cyprus in 2021. This research campaign was performed by Cyprus Atmospheric Observatory (CAO: https://cao.cyi.ac.cy/) and the Unmanned Research Laboratory (USRL, Kezoudi et al., 2021) of the Cyprus Institute (CYI), in collaboration with the Cyprus Atmospheric Remote sensing Observatory (CARO) of the ERATOSTHENES Centre of Excellence (ECoE) with the aim of

190 characterizing dust properties above the island (Kezoudi et al., 2022). During this campaign, measurements were obtained by remote sensing (lidars, ceilometers and sunphotometers) and UAV based instrumentation (optical particle counters, backscatter sondes, and impactors able to collect dust samples). It is essential to have a method to characterize the depolarization for past data in order to make use of the CIMEL lidar in synergy with the rest of the instrumentation, hence the motivation for this paper.
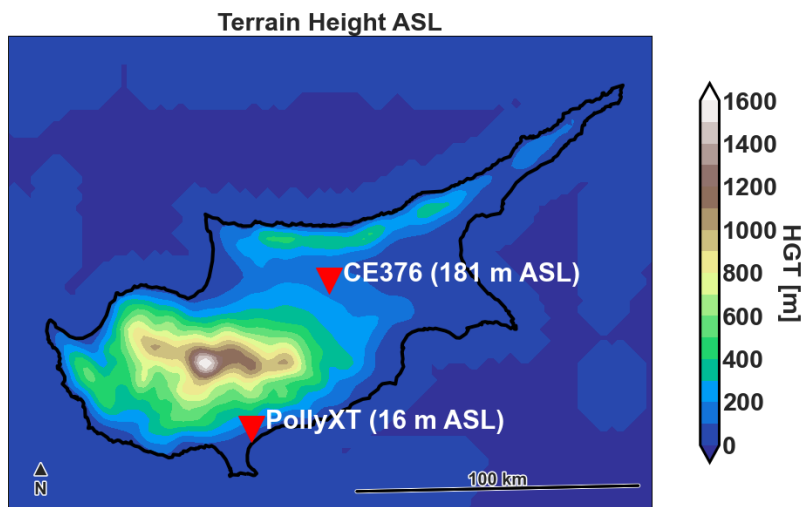
Figure 2. Cyprus topographic map. The red pins indicate the locations of CIMEL CE376 in Nicosia and Polly^{XT} in Limassol.

195 ## 3.2 Polly^{XT} system

Polly^{XT} is a widely used instrument for aerosol observations, which follows calibration and data quality assurance procedures according to EARLINET, hence it serves as our reference system in this paper. It was set up in October 2020 for continuous operation, at Limassol, Cyprus [N34°40′36.01″, E33°2′39.01″] at 11 m asl (location seen on Fig. 2) pointing at 5° off zenith to avoid specular reflections and is part of PollyNET, a network of permanent or campaign-based Polly lidar stations (Baars

200 et al., 2016). Polly^{XT} is a transportable aerosol multiwavelength Raman and polarization lidar that enables the determination of the particle backscatter coefficients at 355, 532, and 1064 nm and extinction coefficients at 355 and 532 nm. In addition, two depolarization channels at 532 and 355 nm are set up to differentiate between spherical and non-spherical aerosol particles from measurements of the PDR. Unlike the CIMEL lidar, Polly^{XT} detects the total scatter light (all polarization planes) and
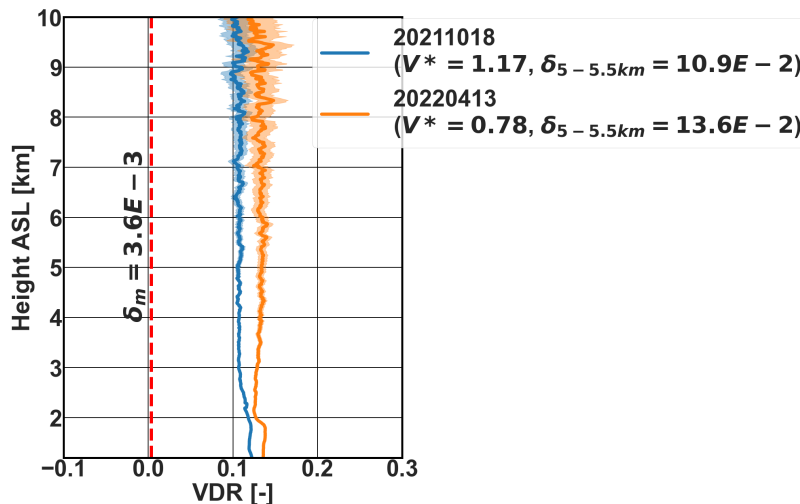
Figure 3. Measured volume depolarization with CIMEL following $\Delta(90°)$ calibration for two cases dominated by molecular scattering above 3 km. Blue for the case from period 1 and orange for period 2. The red dashed line shows the computed based on Behrendt and Nakamura (2002) depolarization ratio at molecular layers.

the cross-polarized light. To characterize the depolarization, Polly^{XT} performs automated $\Delta(90°)$ calibration twice per day (at 02:30 and 16:50 UTC). The calibration is automatically analyzed within the PollyNET Processing Chain (Baars et al. 2016, Yin and Baars 2016). This type of lidar was previously introduced by Althausen et al. (2009) and Engelmann et al. (2016), whilst other publications presented the potential of these systems for monitoring aerosols in Central Asia (Hofer et al., 2017, 2020a, b) and the southermost South America (Jimenez et al., 2020).

Limassol is located on the other side of the Troodos mountain range with respect to Nicosia. Due to the topography, complex aerosol mixtures are observed over Limassol consisting of desert dust arriving from the Sahara or Arabian desert, marine particles, urban pollution and even smoke plumes as it was shown in Mamouri and Nisantzi's work (2013; 2014; 2016; 2016b; 2014; 2015).

In this paper, the systematic errors related to the volume linear depolarization ratio of the Polly^{XT} are taken from the study done by Bravo-Aranda et al. (2016), where the author provides some indications of the systematic errors based on the lidar model of Freudenthaler et al. (2016). Based on that model $\Delta\delta(0.45) = 0.0156$ for dust layers and $\Delta\delta(0.004) = 0.0057$ for molecular range. The considered Polly^{XT} profiles of this paper are presented together with the aforementioned systematic error.

4   Lidar depolarization characterization

In this section, we describe the methodology on how to determine polarization parameters for the CIMEL lidar using the Polly^{XT} as our reference system for selected cases during dust events, for both periods 1 and 2 seen in Table 1. For the

atmospheric depolarization characterization, we selected cases with dust layers that were part of the long distance advection of dust from the nearby deserts. Dust over the island is considered to be fairly homogeneous in the free troposphere and the distance between the Polly^{XT} and CIMEL lidar is much smaller than the distance travelled from source regions. Ideally, an intercomparison should be done with both systems side by side to sample the same air mass. If this is not possible, for example when already existing data need to be corrected, someone has to select the cases carefully. For this paper, data were already available from the Cyprus Fall Campaign 2021, during which the two stations were separated by $\sim$ 60 km. Due to this spatial distance between the two lidars and the mountains in the area, the VDR could change because of atmospheric changes e.g., temperature and relative humidity. In addition, it is recognized that pollution originating from northern African states might impact long-transported dust plumes. Studies, such as Groß et al. (2013), have demonstrated how this pollution can alter the lidar observations, mainly by reducing the depolarization ratio.

Hence, it is important to carefully select the cases for which both lidars measure similar VDR profiles based on the following criteria: (i) dates with dust layers detected above 3 km, to exceed the topographic obstacle of Troodos in the centre of the island, (ii) molecular signal above the dust layer, (iii) only nighttime profiles are selected to improve SNR, (iv) cloud free scenes or high level clouds only and (v) general assessment of the meteorology to confirm the origin of air masses as being due to long range transport. For all the cases used for the determination of polarization parameters, we have performed HYSPLIT (Stein et al., 2015) back trajectories (Fig. 4) to demonstrate that the air masses at arrival heights corresponding to the peak VDR values are produced in long distance and therefore are not affected by local effects. We believe that it is reasonable to neglect local differences for well selected cases of free tropospheric layers having been transported from the same source region for more than 3000 km given the short distance (60 km) between the two stations.

The method is based on some important assumptions. Firstly, we assume that the dust layer VDR is identical above 3 km in the measured profiles by the two systems. The second assumption is that there is no time shift between the two measurements. Only depolarization at 532 nm will be considered from the Polly^{XT} which is the wavelength of the CIMEL lidar depolarization measurements that we wish to characterize.

Before comparing the profiles from the two instruments, we apply time integration and smoothing on the CE376 and Polly^{XT} measurements to a common temporal and vertical range resolution (1 hour and 82.5 m respectively). The timestamps provided in the paper align with the starting moments of each one-hour interval. As last step, we correct for the vertical shift observed on the profiles of the two lidars. This correction aims to remove the altitude difference between the two locations in the case of a sloping layer (more on this correction in Appendix C).

We demonstrate the proposed depolarization characterization approach using profiles from two nights that follow the criteria described before. As the dataset was limited (due to the selection criteria, i.e., dust layer above 3 km), the selected cases are taken from days with uniform dust layers over the island and for which the profiles of the two systems do not seem to be influenced by any local phenomena. The first profile corresponds to 26 November 2021, 22:00 UTC, and it is taken from a 5 day long dust event arriving from the Sahara desert (confirmed with HYSPLIT back trajectories, Fig. 4 a), resulting in a daily average AOD$_{500nm}$ value of 0.14 and 0.08 over Nicosia and Limassol respectively (AERONET, https://aeronet.gsfc.nasa.gov). During this event, one uniform dust layer was observed from 2 up to 4 km. The second profile corresponds to 16 February
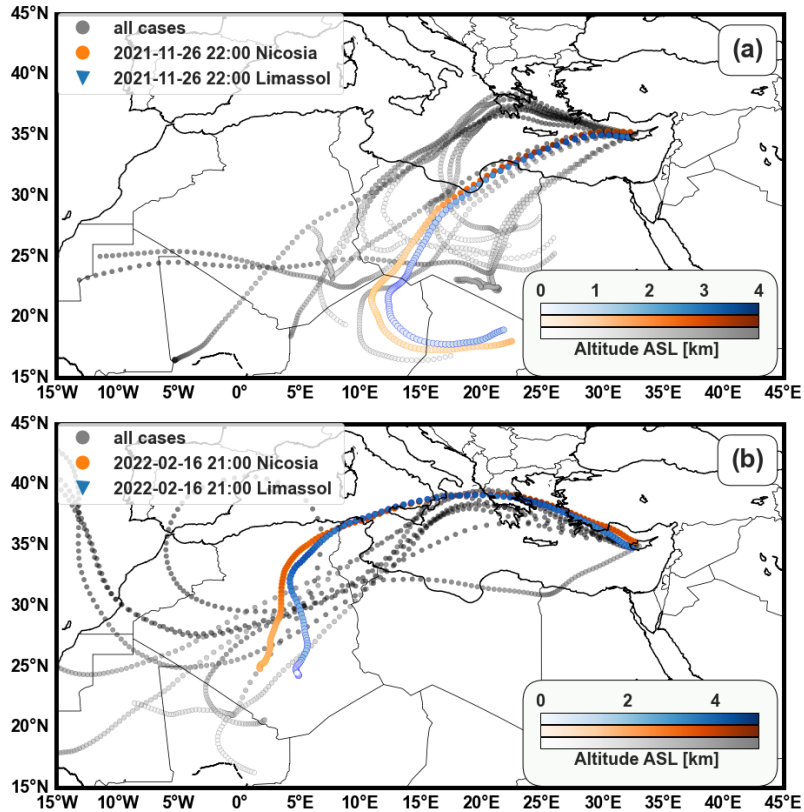
Figure 4. HYSPLIT back trajectories (https://www.ready.noaa.gov/) ending in Nicosia for all the selected cases for the first (a) and second period (b)(the two periods are separated for illustration purposes). The two demonstration cases are highlighted for endpoints in Nicosia (orange) and Limassol (blue). Color scaling indicates the elevation of the layer with light being at ground level and darker increasing altitude. The arrival heights for 26 November 2021, 22:00 UTC correspond to 3.3 km (Nicosia) and 3.1 km (Limassol) and for 16 February 2022, 21:00 UTC, 4.1 km (Nicosia) and 3.9 km (Limassol). The arrival heights are chosen to be at the peak VDR of the dust layer.

2022, 21:00 UTC, and it is extracted from a relatively shorter event (2 day long) during which dust was advected also from the Sahara desert to Cyprus (Fig. 4 b), but this time not as uniform in the vertical direction with some distinct layers seen around 4 km. A cirrus cloud layer was also identified from 6 to 10 km. For the second event, the daily AOD_{500nm} average over Nicosia was 0.20, whilst no data were available from Limassol's sunphotometer. The VDR profile time-series of the days from which we extracted the timestamps are seen in Fig. 5. From this Figure we see how similar the VDR is at the high depolarizing layers.

4.1 Two-parameter depolarization characterization

In order to find the gain ratio K^* and cross-talk g we create a system of equations following Eq. 10 using our reference measurements of the average volume depolarization δ_d^{ref} of a dust layer and the computed molecular depolarization, $\delta_m = 0.0036$ for the CIMEL lidar as mentioned also in Section 3.1. The calculation of the polarization parameters does not utilize
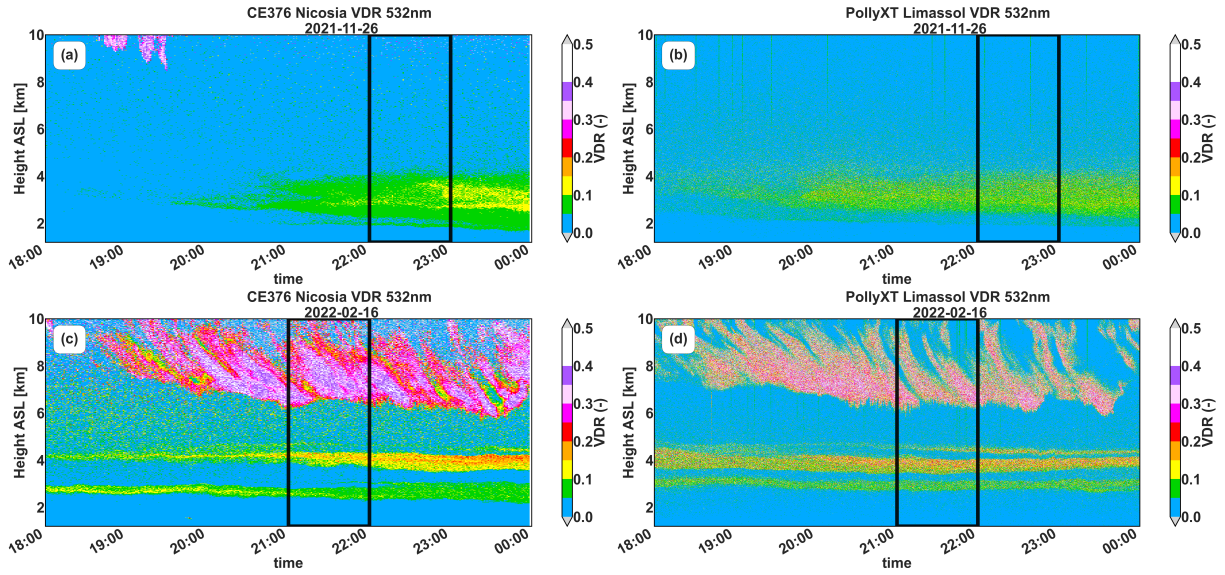
Figure 5. VDR observations by CE376 lidar in Nicosia and Polly XT in Limassol for 26 November 2021 (a, b) and 16 February 2022 (c, d) in 1 minute time resolution. Sub-figures a and c present the VDR from CE376 after the characterization of the polarization parameters using the two-parameter approach. Black lines indicate the 1 hour average interval of the demonstrated cases.

265 signals from the reference lidar in the Rayleigh-scattering layers as VDR at these layers is instrument-dependent (depends on the receiver's bandwidth). Instead, we rely on the model of the molecular linear depolarization ratio by Behrendt and Nakamura (2002). For every examined profile, we select δ_d^{ref} from the reference instrument and the channel signal ratio of dust (δ_d^*) and of the molecular layer (δ_m^*) from the CIMEL instrument in the corresponding ranges. By applying Eq. 10 to these layers:

$$\delta_{ref}^d = \frac{\delta_d^*}{K^*} - g, \tag{11}$$

270 $$\delta_m = \frac{\delta_m^*}{K^*} - g. \tag{12}$$

With two unknowns and two equations, we can solve for K^* and g:

$$K^* = \frac{\delta_d^* - \delta_m^*}{\delta_{ref}^d - \delta_m} \tag{13}$$

$$g = \frac{\delta_m^* \delta_{ref}^d - \delta_d^* \delta_m}{\delta_d^* - \delta_m^*} \tag{14}$$

275   Fig. 6 shows the application of the method described above for the cases considered in the first and second periods. In this figure, the resulting VDR profile (δ_2) is compared to the reference Polly^{XT} VDR profile (δ_{ref}) and the CIMEL VDR profile (δ_1) calculated based on the $\Delta(90)^\circ$ method described in Section 3.1. For the first case (26 November 2021, 22:00 UTC) δ_{ref}^d and δ_d^* are selected in the range h_{δ_d} = 3.1–3.4 km. The molecular range δ_m^* for this case is chosen between $h_{\delta_m^*}$ = 6–6.5 km. The VDR value at the molecular range after the correction is reduced from 0.158 $\pm$ 0.011 to 0.0033 $\pm$ 0.0067. In the dust

280   layer δ_2 = 0.0829$\pm$ 0.0012 and δ_{ref} = 0.08319 $\pm$ 0.00087 compared to δ_1= 0.2840$\pm$ 0.0019. The offset seen in the molecular VDR profile from the reference system, is expected due to the unique interference filters of each instrument (molecular VDR is strongly influenced by the instrument specification).

For the second case (16 February 2022, 21:00 UTC), δ_{ref}^d and δ_d^* are selected in the range h_{δ_d} = 4–4.3 km, whilst molecular range δ_m^* is selected between $h_{\delta_m^*}$ = 5.5– 6 km. In this range, the molecular VDR reduced from 0.1151 $\pm$ 0.0056 to 0.0013

285    $\pm$ 0.0116, after applying the two-parameter method which is not far from the computed δ_m. At the reference dust layer, δ_2 = 0.161 $\pm$ 0.011 and δ_{ref} = 0.160 $\pm$ 0.013 where before the correction δ_1 = 0.1930 $\pm$ 0.0051. VDR values in the lowest ranges (<1.6 km) of 16 February 2022, 21:00 UTC, appear to be slightly negative. These unphysical negative values are indicative of a slightly overestimated g. When the uncertainty on g is accounted for (see error bars calculated according to Appendix D), the results are compatible with a VDR larger or equal to zero within one standard deviation of the derived VDR. Hence, these

290   negative values are indicative of the uncertainty on g but are acceptable in this case within the error bars. The determined polarization parameters correct the depolarization values (δ_2) both at high and low depolarizing layers, which is confirmed by the presented cases where the VDR at the molecular layers approaches the computed with only small deviations.
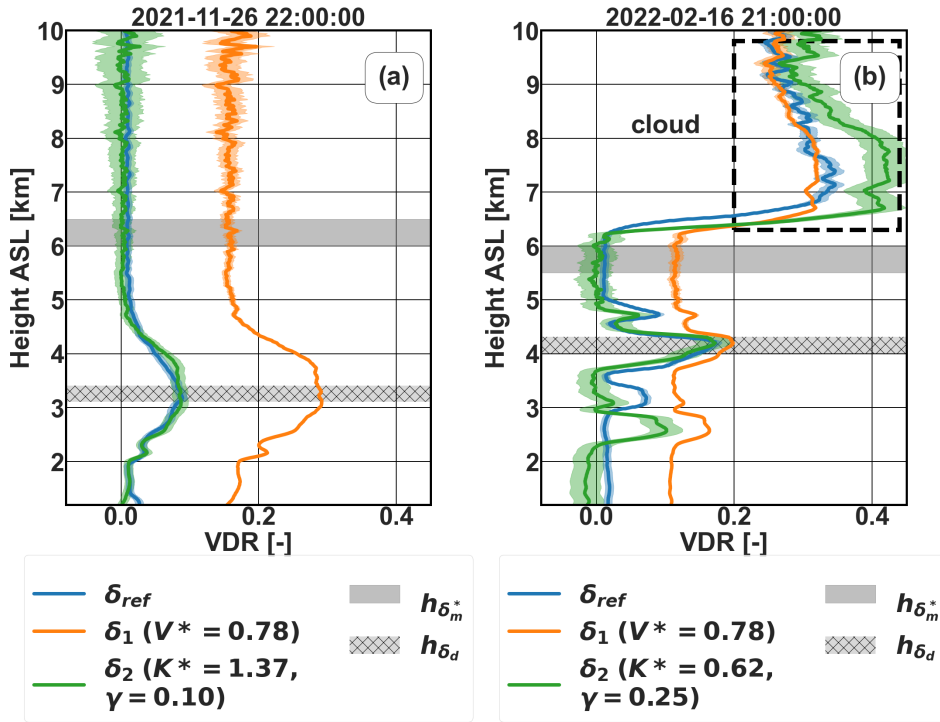
Figure 6. VDR profiles calculated using the two-parameter approach for 26 November 2021, 22:00 UTC (a) corresponding to the first period and 16 February 2022, 21:00 UTC (b) corresponding to the second period using the two-parameter approach. Non-corrected CIMEL lidar VDR profile using the $\Delta(90°)$ calibration factors (δ_1) and corrected profile (δ_2) using the two-parameter approach are compared to the reference Polly^{XT} lidar profile (δ_{ref}). The shaded regions indicate the reference ranges used for dust and the molecular layers. Systematic errors of the reference instrument are shown with a blue shade and the statistical uncertainty of the CIMEL profiles are shown with the orange (non-corrected δ_1) and green (corrected δ_2) shaded areas.

	Period 1			Period 2		
$\Delta(90°)$ calibration	V* = 1.17			V* = 0.78		
two-parameter	K* = 1.29 ± 0.10	g = 0.1034 ± 0.0069		K* = 0.725 ± 0.050	g = 0.204 ± 0.025	
three-parameter	K* = 1.350 ± 0.080	g = 0.1043 ± 0.0061	e = 0.30 ± 0.48	K* = 0.713 ± 0.045	g = 0.226 ± 0.021	e = -0.09 ± 0.18

Table 2. Average polarization parameters for each examined period given with the standard deviation. All values are rounded to two significant figures for the standard deviation.

Polarization parameters were calculated for all the chosen profiles during the two specified periods. The resulting polarization parameters are seen in Fig. 7 with error bars representing their variation within the selected comparison ranges $h_{\delta_m^*}$ and h_{δ_d}. As depicted in Fig. 7, the parameter timeseries indicate consistent values with slight fluctuations around their mean. This stability allows us to employ average polarization parameters seen in Table 2 for the specified periods. By comparing the average value of g from the table to the values in Fig. 6b, it is evident that the calculated g value for 16 February 2022, 21:00 UTC
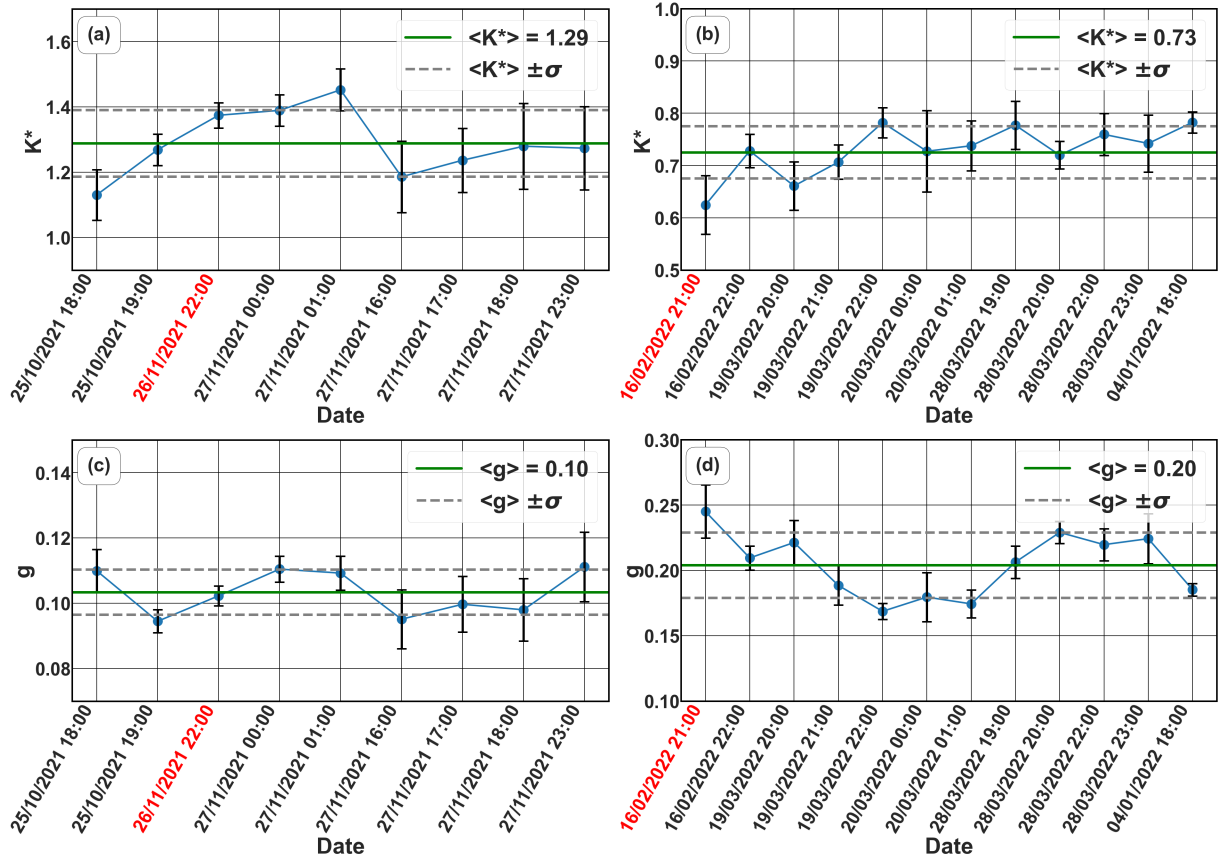
Figure 7. Two-parameter approach derived polarization parameters vs time for the first period (a,c) and second period (b,d). The error bars represent the derived parameter's variation within the selected comparison ranges $h_{\delta_m^*}$ and h_{δ_d}. The average polarization parameter value and its standard deviation in the whole period is given with green and dashed grey lines respectively. The timestamps of the cases shown in Fig. 6 are highlighted in red colour.

was overestimated ($g = 0.25$ compared to $g = 0.20$). This is reflected in the slightly negative values in the lowest ranges of the graph in Fig. 6b. Figures 8 show the VDR profiles using the average polarization parameters for the two individual cases shown previously in Fig. 6. There is no important effect on the profiles from the application of the average parameters, with low and high depolarizing layers being represented well. Any observed variations remain within the uncertainty of the method. The shaded area around the average-parameter corrected profile (brown) shown in Fig. 8 represents the errors associated with the variability of the K^* and g parameters during the selected periods and was calculated as described in Appendix D.

4.2 Three-parameter depolarization characterization

In the previous simplified approach, we neglected the e cross-talk constant. In principle, this approximation can introduce errors at the dust and cloud layers (large δ) and we expect the three-parameter approach to fill this gap. The exception to this is
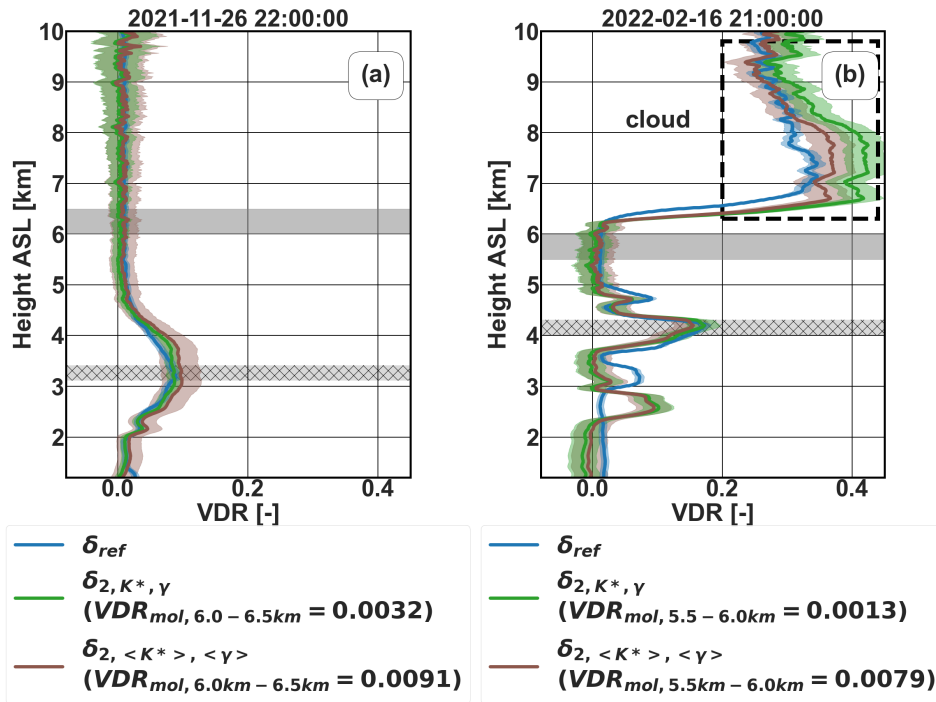
Figure 8. VDR profiles calculated using the two-parameter approach for 26 November 2021, 22:00 UTC (a) and 16 February 2022, 21:00 UTC (b) using the profile-specific (blue) and the average (orange) polarization parameters for the two periods. Systematic errors of the reference instrument are shown with a blue shade and the statistical uncertainty of the corrected profile δ_2 using the average polarization parameters is shown with a brown shade.

for lidar systems where e is close to 0.

In the three-parameter depolarization characterization, we retrieve all the constants, namely g, e and K^*. As now there are three unknowns (Eq. 8), determining the cross-talk constant e requires additional input from the measured aerosol column. In addition to the dust and the molecular layer used in the two-parameter approach (δ_{d_1} and δ_m), we can use a second dust layer or/and a high-level ice cloud (δ_{d_2}). Using ice cloud data requires caution due to potential differences in ice crystal orientation measured between systems and due to the distance between the two lidars which may capture different parts of the cloud. Furthermore, the way the lidar is pointed, especially when dealing with oriented ice crystals, and the possibility of multiple scattering effects, highlight the importance of carefully interpreting the results when using ice clouds. We apply this here for an illustrative purpose in one case only but we advocate using two aerosol layers whenever possible. The resulting three-parameter equations are:

$$\delta_{ref_i} = \frac{\delta_{d_i}^* - K^* g}{K^* - e\,\delta_{d_i}^*} \; (\text{i} = 1,2) \tag{15}$$

$$\delta_m = \frac{\delta_m^* - K^* g}{K^* - e\,\delta_m^*} \tag{16}$$

This approach introduces an additional constraint to the determination of the parameters. The main reason is that identifying cases with two layers with different depolarization properties measured by both instruments can be rare. As a result of this, reducing the number of selected cases increases the uncertainty of the derived polarization parameters. Moreover, the two independent layers can be advected in a different way and therefore it is not necessarily possible to use the same vertical shift correction for both.

During the first period, it was really difficult to identify profiles with two layers above 3 km, mainly because the dust events remained at lower altitudes. However, with only a few cases we derived the polarization parameters seen in Table 2.

For the second period, more cases passed the selection criteria mentioned at the beginning of Section 4. Fig. 9 shows the time dependence of the resulting parameters for the second period with error bars representing their variance within the comparison ranges $h_{\delta_m^*}$ and $h_{\delta_{d1,2}}$.

Comparing the polarization parameters from the two approaches (two-parameter vs three-parameter) in Table 2, g and K^* remained almost unchanged, which satisfies our expectations that the effect of g dominates the low depolarization layers. This is also confirmed by the values of e which are compatible with zero when considering their associated uncertainties. In Fig. 10, the VDR profiles from the two approaches are compared to give a full picture of the vertical deviations. The three-parameter approach tends to yield smaller VDR across the entire profile range, and negative values outside the dust and cloud layers. Additionally, the polarization parameters derived using the three-parameter approach exhibit increased variability, compared to the 2-parameter approach, as indicated by the error bars in Fig. 10. The shaded error bar region in Fig. 10, representing the uncertainty associated with the three-parameter method (explained in Appendix D), highlights that the discrepancies observed between the two methods and also the occurrence of negative values can be explained by the uncertainty on g and e (1 standard deviation). Following these results, we prefer to keep things simple with the two-parameter approach and neglect the effect of e for this instrument.
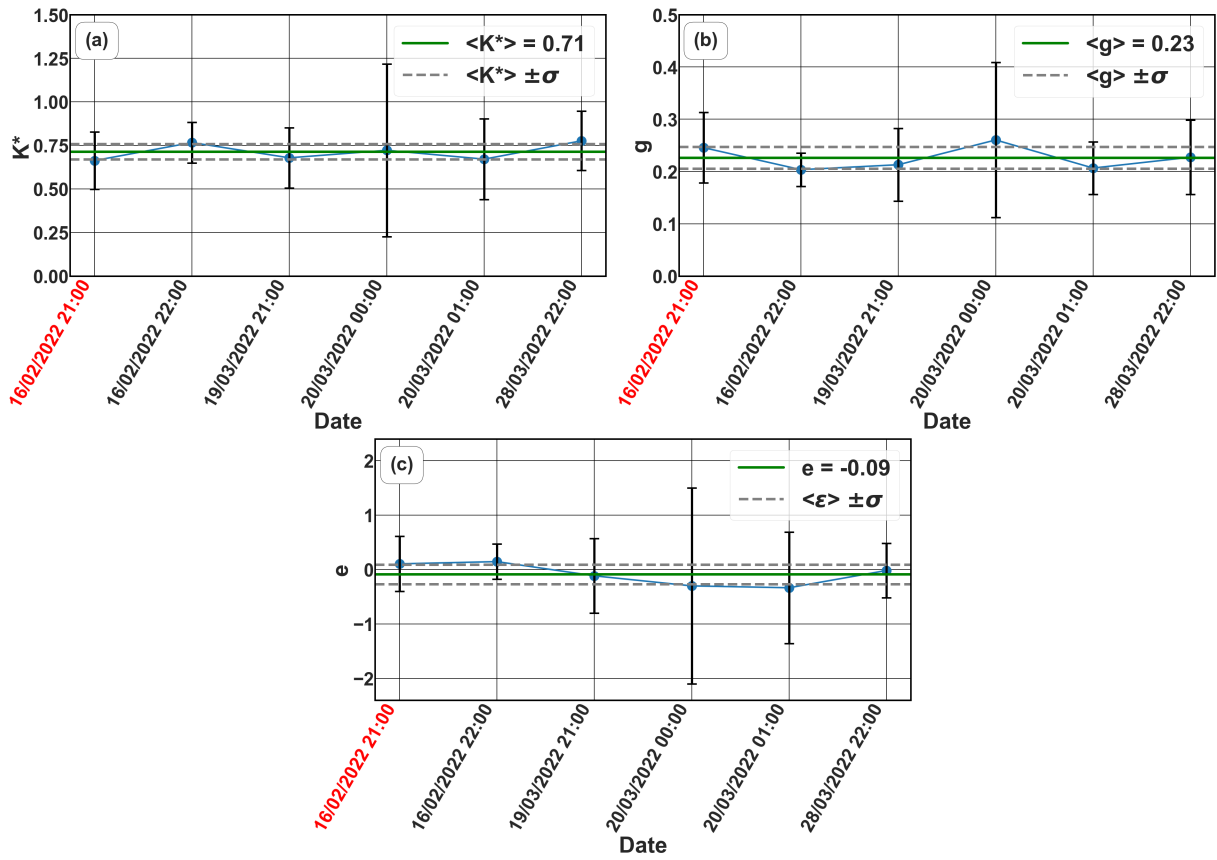
Figure 9. Polarization parameters vs time for the second period for the three-parameter approach. The error bars represent the derived parameter's variation within the selected comparison ranges $h_{\delta_m^*}$ and $h_{\delta_{d1,2}}$
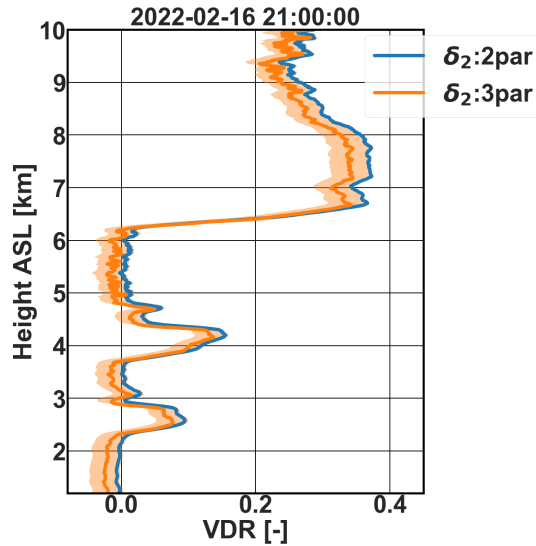
Figure 10. VDR profiles for 16 February 2022, 21:00 UTC calculated using the 2-parameter (blue) and the 3-parameter polarization parameters. The shaded error bar area corresponds to the 3-parameter method uncertainty.

4.3 Effective angle of rotation between receiver and emitter

In Freudenthaler et al. (2009) the characterisation of depolarization is achieved through knowledge of the channel gain ratio, the beamsplitter transmittances and reflectances, and the angle of rotation ϕ between the polarization of the emitter with respect to the frame of reference of the receiver. With the method presented here, instead, the characterisation is achieved through the determination of the parameters K^*, g, and e. These two representations can be made mathematically equivalent, as shown in Appendix A, and this opens an opportunity to evaluate the angle ϕ from Eq. A3, using the derived value of g and assuming that the beamsplitter parameters $R_p = 1 - T_p$ and $R_s = 1 - T_s$ provided by the manufacturer and given in Table 1 are correct. When doing this exercise, we evaluate that $\phi = (71 \pm 1)°$ and $\phi = (66 \pm 1)°$ for periods 1 and 2, respectively. It is to be noted that the derived angle is not the true angle of rotation, given that in our instrument the angle of rotation is minimized and made to be close to 0° by rotation of a HWP in the optical path to maximize the co-polar signal for molecular layers (see Section 3.1). We will therefore call ϕ the effective angle of rotation, being a useful parameter to characterise the residual cross talk in the system. We recall, moreover, that different beamsplitters were used for both periods and yet the evaluated ϕ of $66 - 71°$ does not undergo a huge variation: this may suggest that the issue more likely resides in the emitter (laser depolarization purity) or an incorrect characterization of the PBS or additional diattenuation due to other optical components. Note that the calculations in this paper are based on the mathematical model described in Section 2, which does not account for the characteristics of the components of the lidar system. The fact that we find such a large effective angle of rotation shows that some unknown error sources in the CIMEL lidar are causing the large cross-talk that we observe.

5 Conclusions

We have presented and demonstrated a method for determining the polarization parameters using observations from a reference instrument at a nearby location. Our approach accounts for the cross-talk between the co-polar and cross-polar channels by employing a set of equations that contain three-parameters, K^*, g and e, using observations from a reference lidar. We examined the ability of this method to characterize VDR observations from a lidar for which the standard calibration procedures could not fully account for the cross-talk, by utilizing VDR measurements from a reference and previously calibrated lidar. The aim is to obtain the correct depolarization of dust layers and approach the calculations based on Behrendt and Nakamura (2002) for the molecular layers.

Results are shown for both a simplified version of this method, the two-parameter approach, where the cross-polar interference into the co-polar channel (e) is neglected and the three-parameter approach where all parameters are to be retrieved. As a whole, the depolarization characterization approach of this paper corrects the depolarization values of both high (i.e., dust) and low depolarizing (i.e., molecular) layers and permits the estimation of the cross-talk parameters. The reliability of the atmospheric depolarization characterization method is supported by observing reduced discrepancies in VDR when compared to expected VDR values at molecular layers. The VDR relative difference to the reference observations at dust layers is less than 1% after the application of the two-parameter approach.

The application of the three-parameter approach was more challenging, mainly due to the few cases which satisfy the criterion of having two independent aerosol layers above 3 km in one profile. Based on these cases the recalculated parameters K^* and g did not change more than 5%. We found from the results of the three-parameter approach that e was small enough and therefore could be neglected thus justifying the two-parameter approach.

The calculated polarization parameters from different cases (9 and 12 timestamps for the first and second periods respectively) vary little over the examined periods, allowing us to apply average parameters calculated for the specific system for calculating VDR on longer periods, as it was shown in this study. The application of the average instead of the profile specific polarization parameters leads to neglectable differences at the high and low depolarized layers, which is acceptable as it remains within the uncertainty of the method. Nevertheless, the system's degradation could affect the polarization parameters and therefore, it is suggested that these are re-evaluated on a seasonal basis and at every system upgrade. The applied polarization parameters are found to reduce significantly the VDR discrepancies between the tested and the reference lidar in cases where distinct and similar dust layers are observed, thus justifying its retrospective application to be able to use existing valuable data acquired during campaigns.

The EARLINET09 intercomparison of lidars campaign suggests a detailed methodology on the intercomparison approach, requiring all systems to be placed side by side for several days before being deployed at their measuring locations, in order to be able to combine observations from different instruments and techniques (Wandinger , 2016). We need to emphasize that this was not possible in this case, as we are attempting a retrospective characterization of Cyprus 2021 Fall Campaign observations. However, these guidelines should be followed whenever possible, and for the future, we plan an upgrade of the system to have a reliable calibration upfront.

This depolarization characterization method, demonstrated here for the first time, provides a good alternative for systems for which the user doesn't know the values of g and e a priori and therefore can be applied where traditional calibration procedure fails to correct the cross-talk in the depolarization channels. According to Bravo-Aranda et al. (2013), lidar systems which are not well characterized and aligned can lead to large systematic errors in the depolarization values. Reducing the errors related to the depolarization observations will therefore reduce the total uncertainty of aerosol typing studies (e.g., Mamouri and Ansmann, 2014) or mass concentration retrievals (e.g., Mamali et al., 2018), for which particle linear depolarization ratio is a key parameter.

It is noteworthy to highlight that in Freudenthaler's (2016) work, a comprehensive theoretical framework for depolarization calibration was introduced, significantly expanding the scope of influencing quantities and parameters. A different approach for atmospheric calibration would be to apply an intercomparison that takes into account these parameters and includes a more comprehensive error calculation.

Using the presented method, valuable data obtained during the Fall Campaign 2021 in Cyprus (Kezoudi et al., 2022), can be corrected and used for further research on aerosol characteristics and stratification.

Appendix A: How the present treatment of depolarization relates to Freudenthaler et al, 2009

Freudenthaler et al. (2009) treated lidar depolarization extensively and introduced the $\Delta(90°)$ method for calibration, which is nowadays of widespread use and a de facto standard. We relate here their equations to the ones developed in the Section 2. Whereas in Section 2 we don't make any assumptions on the technology employed, the treatment in that paper assumes that the two polarization components are separated in the receiver by means of a polarizing beamsplitter cube (PBS) of known characteristics, and that the emitted beam polarization plane may be rotated with respect to the PBS reference system. We rewrite here their Eq. (9) for convenience:

$$\delta_F^* = V^* \frac{R_p\left(1 + \delta \tan^2 \phi\right) + R_s\left(\tan^2 \phi + \delta\right)}{T_p\left(1 + \delta \tan^2 \phi\right) + T_s\left(\tan^2 \phi + \delta\right)}, \tag{A1}$$

where δ_F^* is the ratio of the two lidar signals, V^* is the channel gain ratio, and ϕ is the angle between the plane of polarization of the laser and the incidence plane of the PBS. R_p, R_s, T_p, T_s indicate the reflectivities and transmittances of the PBS for linearly polarized light parallel (p) and perpendicular (s) to the incidence plane, with $R_p \simeq 1 - T_p$, $T_s \simeq 1 - R_s$. The reason why we use the symbols δ_F^* instead of δ^*, and V^* instead of K^*, will be apparent in the following.

This equation has to be compared to our equation (7). The lidar PBS can be basically installed in two logical configurations: with ϕ close to $0°$ or with ϕ close to $90°$. In the first case, $\delta_F^* = \delta^*$, by comparing Eq. (A1) and Eq. (7) one finds that:

$$K^* = V^* \frac{R_p \tan^2 \phi + R_s}{T_p + T_s \tan^2 \phi} \tag{A2}$$

Note that in the case that $R_s, T_p \ll 1$ (like in the case of CE376) or $R_p, T_s \ll 1$ (like in the cases of other lidars in the literature), Eq. A2 can be reduced to $K^* \simeq V^*$.

$$g = \frac{R_p + R_s \tan^2 \phi}{R_p \tan^2 \phi + R_s} \tag{A3}$$

$$e = \frac{T_p \tan^2 \phi + T_s}{T_p + T_s \tan^2 \phi} \tag{A4}$$

In the case that the system has $\phi = 90°$, then $\delta_F^* = 1/\delta^*$, equations equivalent to the above can be derived with a simple
425   derivation (omitted for brevity), and $V^* \simeq 1/K^*$

Appendix B: How the present treatment of depolarization relates to Freudenthaler et al., 2016

Freudenthaler et al. (2016) provided general formulations for calculating the linear volume depolarization ratio for different
lidar setups considering various error sources stemming from different components from the laser to the detector. The errors can
stem from rotational misalignments and crosstalks. The general formula for volume depolarization ratio is given in equation
430   62 of Freudenthaler et al. (2016) and is:

$$\delta = \frac{\delta^*(G_T + H_T) - (G_R + H_R)}{(G_R - H_R) - \delta^*(G_T - H_T)} \tag{B1}$$

where G_T, G_R, H_T and H_R describe the polarisation crosstalk terms of the lidar setup in the reflected (R) and transmitted
paths (T).

By comparing this equation to to Eq. (10) of this paper one finds that:

435   $$K^* = \frac{G_R - H_R}{G_T + H_T} \tag{B2}$$

$$g = \frac{G_R + H_R}{G_R - H_R} \tag{B3}$$

$$e = \frac{G_T - H_T}{G_T + H_T} \tag{B4}$$

Therefore, the calculation of K^*, g and e can lead to G_T, G_R, H_T and H_R and vice-versa. This means that g and e
parameters obtained through lidar comparison with a reference instrument can be linked to the crosstalk terms computed from
440   the instrument's internal components (if known).

Appendix C: Vertical shift correction due to spatial separation

A vertical shift appears in the comparison of the profiles of the two instruments mainly due to sloping atmospheric layers
between Limassol and Nicosia. This shift can be observed when comparing the most important common dust or cloud layers.

A vertical correction is applied on one of the lidar profiles in order to bring the interesting layers to the same altitudes as the
445 second lidar. An example of this correction is seen in Fig. C1, where we consider a vertical correction of $dh = 0.25$ km for the
selected timestamp.
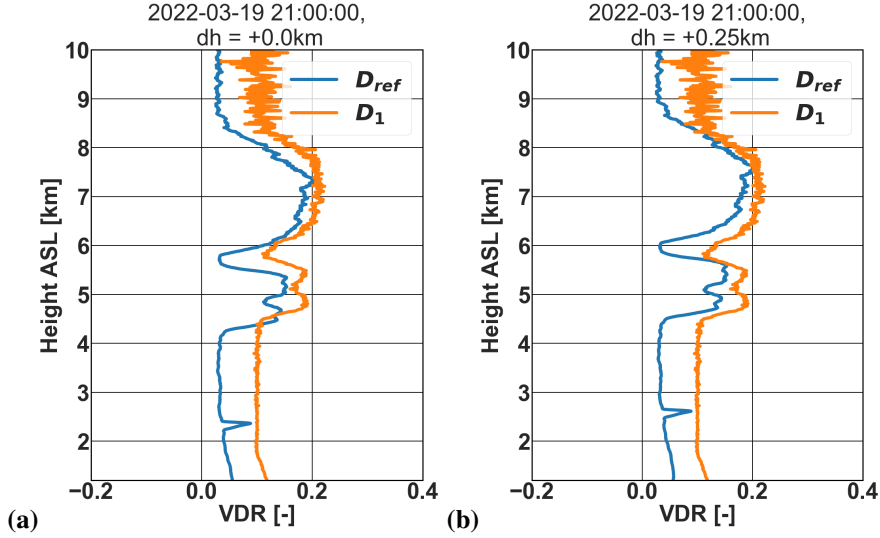
Figure C1. VDR profiles without (left) and with (right) vertical correction.

Appendix D: Uncertainty analysis

The corrected values of δ are subject to the propagation of uncertainty. The uncertainty of the presented two-parameter approach
can be calculated according to GUM (2008) as follows:

450 $$(\Delta\delta)^2 = f(\Delta K^{*2}, \Delta g^2, \Delta\delta^{*2}) = \left[\left(\frac{\Delta\delta^*}{\delta^*}\right)^2 + \left(\frac{\Delta K^*}{K^*}\right)^2\right]\left(\frac{\delta^*}{K^*}\right)^2 + (\Delta g)^2 \tag{D1}$$

$$= \left[\left(\frac{\Delta P^\perp}{P^\perp}\right)^2 + \left(\frac{\Delta P^\|}{P^\|}\right)^2 + \left(\frac{\Delta K^*}{K^*}\right)^2\right]\left(\frac{P^\perp}{P^\| K^*}\right)^2 + (\Delta g)^2$$

In the above equation, ΔK^* and Δg are the statistical uncertainties of the parameters within the chosen interval (e.g. the
standard deviation presented in Table 2). The measurement uncertainty $\Delta P^\perp$ and $\Delta P^\|$ for each polarization channel consists
of the uncertainty of the raw counts signal (P_0) and the background correction (B). As the signal is received by a photon
455 counting detector the distribution of the counts follows Poisson statistics and therefore the standard deviation is given by the
square root of the number of counts in the measured interval (N).

$$\Delta P^{\perp,\|} = \sqrt{(\Delta P_0^2) + (\Delta B^2)} = \sqrt{N + \frac{\sigma(B)^2}{n}} \tag{D2}$$

where $\sigma(B)$ is the standard deviation of the background correction calculated over n = 67 ranges which corresponds to 1 km.

460 These calculations are used for deriving the error bars of the two-parameter correction profiles seen in Figures 6 and 8. The uncertainty of δ in the three-parameter approach is also depended on Δe and therefore $(\Delta\delta)^2 = f(\Delta K^{*2}, \Delta g^2, \Delta e^2, \Delta\delta^{*2})$. We omit the equations here for brevity.

Appendix E: CE376 optomechanical setup

The CE376 consists of two lasers: frequency doubled Nd:YAG emitting at 532 nm and a pulsed laser diode for near-infrared

465 (NIR). The backscattered radiation is collected by a Galilean telescope with a diameter of 100 mm both in emission and reception. In the detection branch after the telescopes the following can be found: a narrow filter for reducing the background light, a half-wave plate to rotate the plane of polarization and a beam splitter cube to separate the parallel and cross-polarized signals received in the 532 nm channel. The signals are recorded by Avalanche Photo Diodes (APDs by SPCM-AQRH modules from Excelitas) at the three reception channels. The APDs are capable of detecting single photon events.
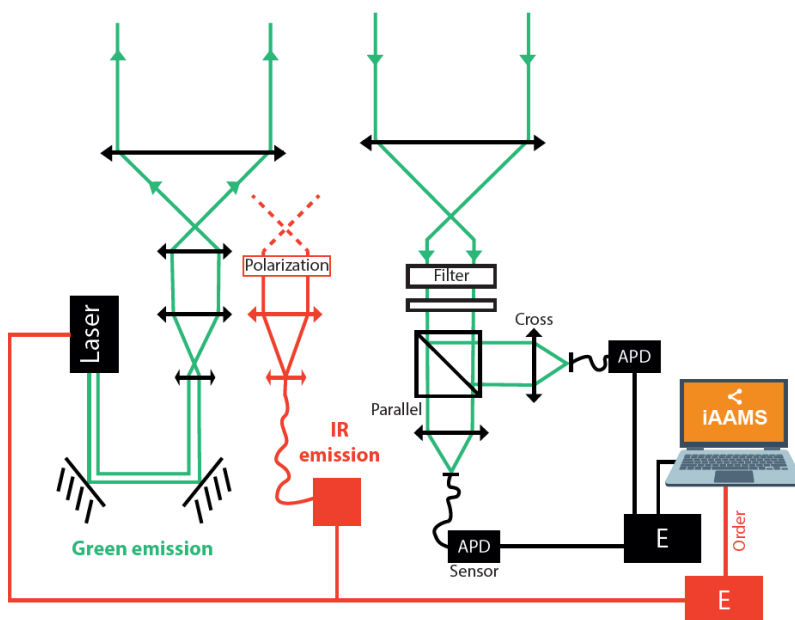
Figure E1. Schematic of the CE376 optomechanical setup.

470 *Author contributions.* AP performed the analysis and all the corrections of the data obtained by CIMEL CE376 in Nicosia. AP and FM performed the on-site calibration in January and February 2022 with the guidance of IP and SV. RM, AN and HB operated and analyzed

the Polly^{XT} data sharing of the relevant cases for comparison and also provided clarifications on Polly^{XT} VDR calculations. AP and FM conceived this research and prepared the initial version of the manuscript. All the co-authors reviewed the manuscript.

Competing interests. The authors declare that they have no conflict of interest

475 *Acknowledgements.* The authors acknowledge EMME-CARE and 'EXCELSIOR'. Also the authors would like to thank CIMEL Electronique for their support in the calibration and testing of the CE376 system. The authors wish to thank Volker Freudenthaler for constructive discussions on lidar depolarization characterization.

Financial support. This publication has been produced within the framework of the EMME-CARE project which received funding from the European Union's Horizon 2020 Research and Innovation Programme, under grant agreement no. 856612 and from the Cyprus Gov-
480 ernment. : ERATOSTHENES: Ecellence Research Centre for Earth Surveillance and Space-Based Monitoring of the Environment H2020 Widespread Teaming project (www.excelsior2020.eu). The 'EXCELSIOR' project has received funding from the European Union's Horizon 2020 research and innovation programme under Grant Agreement No 857510, from the Government of the Republic of Cyprus through the Directorate General for the European Programmes, Coordination and Development and the Cyprus University of Technology. The PollyXT-CYP was funded by the German Federal Ministry of Education and Research (BMBF) via the PoLiCyTa project (grant no. 01LK1603A).
485 The study is supported by 'ACCEPT' project (Prot. No: LOCALDEV-0008) co-financed by the Financial Mechanism of Norway (85%) and the Republic of Cyprus (15%) in the framework of the programming period 2014 - 2021.

References

Althausen, D., Engelmann, R., Baars, H., Heese, B., Ansmann,A., Müller, D., and Komppula, M.: Portable Raman Lidar PollyXT for automated profiling of aerosol backscatter, extinction, and depolarization, J. Atmos. Ocean. Tech., 26, 2366–2378, https://doi.org/10.1175/2009JTECHA1304.1, 2009.

Alvarez, J. M., Vaughan, M. A., Hostetler, C. A., Hunt, W. H., Winker, D. M. : Calibration Technique for Polarization-Sensitive Lidars, J. Atmos. Ocean. Tech., 23(5), 683-699, https://doi.org/10.1175/JTECH1872.1,2006

Ansmann A., Riebesell M., Weitkamp C.: Measurement of atmospheric aerosol extinction profiles with a Raman lidar, Opt Lett., 15(13):746-8, https://doi.org/ 10.1364/ol.15.000746, 1990

Ansmann, A., Riebesell, M., Wandinger, U. et al. Combined raman elastic-backscatter LIDAR for vertical profiling of moisture, aerosol extinction, backscatter, and LIDAR ratio. Appl. Phys. B 55, 18–28 (1992). https://doi.org/10.1007/BF00348608, 1992.

Ansmann, A., Wandinger, U., Riebesell, M., Weitkamp, C., and Michaelis, W.. Independent measurement of extinction and backscatter profiles in cirrus clouds by using a combined Raman elastic-backscatter lidar. Applied optics, 31(33), 7113. https://doi.org/10.1364/AO.31.007113, 1992

Ansmann, A., Engelmann, R., Althausen, D., Wandinger, U., Hu, M., Zhang, Y., and He, Q.: High aerosol load over the Pearl River Delta, China, observed with Raman lidar and Sun photometer, Geophys. Res. Lett., 32, L13815, https://doi.org/10.1029/2005GL023094, 2005.

Ansmann, A., et al.: Ash and fine-mode particle mass profiles from EARLINET-AERONET observations over central Europe after the eruptions of the Eyjafjallajökull volcano in 2010, J. Geophys. Res., 116, D00U02, https://doi.org/doi:10.1029/2010JD015567, 2011.

Ansmann, A., Mamouri, R.-E., Bühl, J., Seifert, P., Engelmann, R., Hofer, J., Nisantzi, A., Atkinson, J. D., Kanji, Z. A., Sierau, B., Vrekoussis, M., and Sciare, J.: Ice-nucleating particle versus ice crystal number concentrationin altocumulus and cirrus layers embedded in Saharan dust:a closure study, Atmos. Chem. Phys., 19, 15087–15115, https://doi.org/10.5194/acp-19-15087-2019, 2019.

Baars, H., Kanitz, T., Engelmann, R., Althausen, D., Heese, B., Komppula, M., Preißler, J., Tesche, M., Ansmann, A., Wandinger, U., Lim, J.-H., Ahn, J. Y., Stachlewska, I. S., Amiridis, V., Marinou, E., Seifert, P., Hofer, J., Skupin, A., Schneider, F., Bohlmann, S., Foth, A., Bley, S., Pfüller, A., Giannakaki, E., Lihavainen, H., Viisanen, Y., Hooda, R. K., Pereira, S. N., Bortoli, D., Wagner, F., Mattis, I., Janicka, L., Markowicz, K. M., Achtert, P., Artaxo, P., Pauliquevis, T., Souza, R. A. F., Sharma, V. P., van Zyl, P. G., Beukes, J. P., Sun, J., Rohwer, E. G., Deng, R., Mamouri, R.-E., and Zamorano, F.: An overview of the first decade of PollyNET: an emerging network of automated Raman-polarization lidars for continuous aerosol profiling, Atmos. Chem. Phys., 16, 5111–5137, https://doi.org/10.5194/acp-16-5111-2016, 2016.

Baars, H., Ansmann, A., Ohneiser, K., Haarig, M., Engelmann, R., Althausen, D., Hanssen, I., Gausa, M., Pietruczuk, A., Szkop, A., Stachlewska, I. S., Wang, D., Reichardt, J., Skupin, A., Mattis, I., Trickl, T., Vogelmann, H., Navas-Guzmán, F., Haefele, A., Acheson, K., Ruth, A. A., Tatarov, B., Müller, D., Hu, Q., Podvin, T., Goloub, P., Veselovskii, I., Pietras, C., Haeffelin, M., Fréville, P., Sicard, M., Comerón, A., Fernández García, A. J., Molero Menéndez, F., Córdoba-Jabonero, C., Guerrero-Rascado, J. L., Alados-Arboledas, L., Bortoli, D., Costa, M. J., Dionisi, D., Liberti, G. L., Wang, X., Sannino, A., Papagiannopoulos, N., Boselli, A., Mona, L., D'Amico, G., Romano, S., Perrone, M. R., Belegante, L., Nicolae, D., Grigorov, I., Gialitaki, A., Amiridis, V., Soupiona, O., Papayannis, A., Mamouri, R.-E., Nisantzi, A., Heese, B., Hofer, J., Schechner, Y. Y., Wandinger, U., and Pappalardo, G.: The unprecedented 2017–2018 stratospheric smoke event: decay phase and aerosol properties observed with the EARLINET, Atmos. Chem. Phys., 19, 15183–15198, https://doi.org/10.5194/acp-19-15183-2019, 2019.

Basart, S., Nickovic, S., Terradellas, E., Cuevas, E., García-Pando, C.P., García-Castrillo, G., Werner, E., Benincasa, F. : The WMO SDS-WAS Regional Center for Northern Africa, Middle East and Europe. E3S Web of Conferences. 99. 04008, https://doi.org/10.1051/e3sconf/20199904008, 2019.

Behrendt, A. and Nakamura T.: Calculation of the calibration constant of polarization lidar and its dependency on atmospheric temperature. Opt. Express 10, 805–817. https://doi.org/10.1364/OE.10.000805, 2002.

Belegante, L., Bravo-Aranda, J. A., Freudenthaler, V., Nicolae, D., Nemuc, A., Ene, D., Alados-Arboledas, L., Amodeo, A., Pappalardo, G., D'Amico, G., Amato, F., Engelmann, R., Baars, H., Wandinger, U., Papayannis, A., Kokkalis, P., and Pereira, S. N.: Experimental techniques for the calibration of lidar depolarization channels in EARLINET, Atmos. Meas. Tech., 11, 1119–1141, https://doi.org/10.5194/amt-11-1119-2018, 2018.

Bösenberg, J. and Matthias, V.: Earlinet: A European aerosol research lidar network to establish an aerosol climatology. Report. Max-Planck-Institut fur Meteorologie. 348. 1-191, 2003.

Bravo-Aranda, J. A., Navas-Guzman, F., Guerrero-Rascado, J. L., Pérez-Ramírez, D., Granados-Munoz, M. J., and Alados-Arboledas, L.: Analysis of lidar depolarization calibration procedure and application to the atmospheric aerosol characterization, Int. J. Remote Sens., 34, 3543–3560, https://doi.org/10.1080/01431161.2012.716546, 2013

Bravo-Aranda, J. A., Belegante, L., Freudenthaler, V., Alados-Arboledas, L., Nicolae, D., Granados-Muñoz, M. J., Guerrero-Rascado, J. L., Amodeo, A., D'Amico, G., Engelmann, R., Pappalardo, G., Kokkalis, P., Mamouri, R., Papayannis, A., Navas-Guzmán, F., Olmo, F. J., Wandinger, U., Amato, F., and Haeffelin, M.: Assessment of lidar depolarization uncertainty by means of a polarimetric lidar simulator, Atmos. Meas. Tech., 9, 4935–4953, https://doi.org/10.5194/amt-9-4935-2016, 2016.

Brogniez, C., Santer, R., Diallo, B. S., Herman, M., Lenoble, J., and Jäger, H. : Comparative observations of stratospheric aerosols by ground-based lidar, balloon-borne polarimeter, and satellite solar occultation, J. Geophys. Res., 97(D18), 20805– 20823, https://doi.org/10.1029/92JD01919 1992.

Cairo, F., Di Donfrancesco, G., Adriani, A., Lucio, P. and Federico, F. : Comparison of various linear depolarization parameters mea- sured by lidar. Appl. Opt. 38, 4425–4432, https://doi.org/10.1364/ao.38.004425, 1999.

Chazette, P., Dabas, A., Sanak, J., Lardier, M., and Royer, P.: French airborne lidar measurements for Eyjafjallajökull ash plume survey, Atmos. Chem. Phys., 12, 7059–7072, https://doi.org/10.5194/acp-12-7059-2012, 2012.

Di Girolamo, P., De Rosa, B., Summa, D., Franco, N. and Veselovskii, I.: Measurements of aerosol size and microphysical properties: A comparison between Raman lidar and airborne sensors. J. Geophys. Res. Atmos. , 127, e2021JD036086. https://doi.org/10.1029/2021JD036086, 2022.

Di Iorio, T., di Sarra, A., Junkermann, W., Cacciani, M., Fiocco, G., and Fuà, D.: Tropospheric aerosols in the Mediterranean: 1. Microphysical and optical properties, J. Geophys. Res., 108, 4316, https://doi.org/10.1029/2002JD002815, 2003.

Engelmann, R., Kanitz, T., Baars, H., Heese, B., Althausen, D., Fahrwald, A., Wandinger, U., Komppula, M., Stachlewska, I., Amiridis, V., Marinou, E., Mattis, I., Linné, H., Ansmann, A.: The automated multiwavelength Raman polarization and water-vapor lidar PollyXT: The neXT generation. Atmos. Meas. Tech., 9. 1767-1784, https://doi.org/10.5194/amt-9-1767-2016, 2016.

Frederick G. F.: Analysis of atmospheric lidar observations: some comments, Appl. Opt. 23, 652–653, https://doi.org/10.1364/AO.23.000652, 1984.

Ferrare, R. A., Melfi, S. H., Whiteman, D. N., Evans, K. D., Poellot, M., and Kaufman, Y. J.: Raman lidar measurements of aerosol extinction and backscattering: 2. Derivation of aerosol real refractive index, single-scattering albedo, and humidification factor using Raman lidar and aircraft size distribution measurements, J. Geophys. Res., 103(D16), 19673– 19689, https://doi.org/10.1029/98JD01647, 1998.

Floutsi, A. A., Baars, H., Engelmann, R., Althausen, D., Ansmann, A., Bohlmann, S., Heese, B., Hofer, J., Kanitz, T., Haarig, M., Ohneiser, K., Radenz, M., Seifert, P., Skupin, A., Yin, Z., Abdullaev, S. F., Komppula, M., Filioglou, M., Giannakaki, E., Stachlewska, I. S., Janicka, L., Bortoli, D., Marinou, E., Amiridis, V., Gialitaki, A., Mamouri, R.-E., Barja, B., and Wandinger, U.: DeLiAn – a growing collection of depolarization ratio, lidar ratio and Ångström exponent for different aerosol types and mixtures from ground-based lidar observations, Atmos. Meas. Tech., 16, 2353–2379, https://doi.org/10.5194/amt-16-2353-2023, 2023.

Fowler, L. D., and Randall, D. A.: Interactions between cloud microphysics and cumulus convection in a general circulation model. J. Atmos. Sci., 59(21), 3074–3098, https://doi.org/10.1175/1520-0469(2002)059<3074:IBCMAC>2.0.CO;2, 2002.

Freudenthaler, V., Esselborn, M., Wiegner, M., Heese, B., Tesche, M., Ansmann, A., Muller, D., Althausen, D., Wirth, M., Fix, A., Ehret, G., Knippertz, P., Toledano, C., Gasteiger, J., Garhammer, M., and Seefeldner, M.: Depolarization ratio profiling at several wavelengths in pure Saharan dust during SAMUM 2006, Tellus B, 61, 165–179, https://doi.org/10.1111/j.1600-0889.2008.00396.x, 2009.

Freudenthaler, V.: About the effects of polarising optics on lidar signals and the Δ90 calibration, Atmos. Meas. Tech., 9, 4181–4255, https://doi.org/10.5194/amt-9-4181-2016, 2016.

JCGM 100:2008 Evaluation of Measurement Data—Guide to the Expression of Uncertainty in Measurement.

Gimmestad, G. G. . Reexamination of depolarization in lidar measurements. Applied Optics, 47(21), 3795. https://doi.org/10.1364/ao.47.003795, 2008.

Groß, S., Tesche, M., Freudenthaler, V., Toledano, C., Wiegner, M., Ansmann, A., Althausen, D., and Seefeldner, M.: Characterization of Saharan dust, marine aerosols and mixtures of biomass burning aerosols and dust by means of multi-wavelength depolarization- and Raman-measurements during SAMUM-2, Tellus B, 63, 706–724, https://doi.org/10.1111/j.1600-0889.2011.00556.x, 2011.

Groß, S., Esselborn, M., Abicht, F., Wirth, M., Fix, A., and Minikin, A.: Airborne high spectral resolution lidar observation of pollution aerosol during EUCAARI-LONGREX, Atmos. Chem. Phys., 13, 2435–2444, https://doi.org/10.5194/acp-13-2435-2013, 2013.

Hofer, J., Althausen, D., Abdullaev, S. F., Makhmudov, A. N., Nazarov, B. I., Schettler, G., Engelmann, R., Baars, H., Fomba, K. W., Müller, K., Heinold, B., Kandler, K., and Ansmann, A.: Long-term profiling of mineral dust and pollution aerosol with multiwave-length polarization Raman lidar at the Central Asian site of Dushanbe, Tajikistan: case studies, Atmos. Chem. Phys., 17, 14559–14577, https://doi.org/10.5194/acp-17-14559-2017, 2017.

Hofer, J., Ansmann, A., Althausen, D., Engelmann, R., Baars, H., Abdullaev, S. F., and Makhmudov, A. N.: Long-term profiling of aerosol light extinction, particle mass, cloud condensation nuclei, and ice-nucleating particle concentration over Dushanbe, Tajikistan, in Central Asia, Atmos. Chem. Phys., 20, 4695–4711, https://doi.org/10.5194/acp-20-4695-2020, 2020.

Hofer, J., Ansmann, A., Althausen, D., Engelmann, R., Baars, H., Fomba, K. W., Wandinger, U., Abdullaev, S. F., and Makhmudov, A. N.: Optical properties of Central Asian aerosol relevant for spaceborne lidar applications and aerosol typing at 355 and 532 nm, Atmos. Chem. Phys., 20, 9265–9280, https://doi.org/10.5194/acp-20-9265-2020, 2020.

Hoffmann, A., Ritter, C., Stock, M., Maturilli, M., Eckhardt, S., Herber, A., and Neuber, R.: Lidar measurements of the Kasatochi aerosol plume in August and September 2008 in Ny-Ålesund, Spitsbergen. J. Geophys. Res. Atmos. , 115(19), 1–12, https://doi.org/10.1029/2009JD013039, 2010.

IPCC, 2021: Climate Change 2021: The Physical Science Basis. Contribution of Working Group I to the Sixth Assessment Report of the Intergovernmental Panel on Climate Change [Masson-Delmotte, V., P. Zhai, A. Pirani, S.L. Connors, C. Péan, S. Berger, N. Caud, Y. Chen, L. Goldfarb, M.I. Gomis, M. Huang, K. Leitzell, E. Lonnoy, J.B.R. Matthews, T.K. Maycock, T. Waterfield, O. Yelekçi, R. Yu, and B. Zhou (eds.)]. Cambridge University Press, Cambridge, United Kingdom and New York, NY, USA, 2391 pp., https://doi.org/10.1017/9781009157896, 2021.

Jimenez, C., Ansmann, A., Engelmann, R., Donovan, D., Malinka, A., Schmidt, J., Seifert, P., and Wandinger, U.: The dual-field-of-view polarization lidar technique: a new concept in monitoring aerosol effects in liquid-water clouds – theoretical framework, Atmos. Chem. Phys., 20, 15247–15263, https://doi.org/10.5194/acp-20-15247-2020, 2020.

Kezoudi, M., Keleshis, C., Antoniou, P., Biskos, G., Bronz, M., Constantinides, C., Desservettaz, M., Gao, R.-S., Girdwood, J., Harnetiaux, J., Kandler, K., Leonidou, A., Liu, Y., Lelieveld, J., Marenco, F., Mihalopoulos, N., Močnik, G., Neitola, K., Paris, J.-D., Pikridas, M., Sarda-Esteve, R., Stopford, C., Unga, F., Vrekoussis, M., Sciare, J.: The Unmanned Systems Research Laboratory (USRL): A New Facility for UAV-Based Atmospheric Observations. Atmosphere 2021, 12, 1042, https://doi.org/10.3390/atmos12081042, 2021.

Kezoudi, M., Papetta, A., Marenco, F., Keleshis, C., Kandler, K., Girdwood, J., Stopford, C., Wienhold, F., Ru-Shan, G., and Sciare, J.: Profiling mineral dust with UAV-based in-situ instrumentation (Cyprus Fall campaign 2021), EGU General Assembly 2022, Vienna, Austria, 23–27 May 2022, EGU22-11209, https://doi.org/10.5194/egusphere-egu22-11209, 2022.

Kiriakidis, P., Gkikas, A., Papangelis, G., Kushta, J., Christoudias, T., Drakaki, E., Proestakis, E., Marinou, E., Gialitaki, A., Kampouri, A., Spyrou, C., Benedetti, A., Rennie, M., Straume, A. G., Retscher, C., Dandocsi, A., Sciare, J., and Amiridis, V.: The impact of assimilating AEOLUS wind data on regional Aeolian dust model simulations using WRF-Chem., EGU General Assembly 2022, Vienna, Austria, 23–27 May 2022, https://doi.org/10.5194/egusphere-egu22-980, 2022.

James D. Klett: Lidar inversion with variable backscatter/extinction ratios. Appl. Opt. 24, 1638-1643, https://doi.org/10.1364/AO.25.000833, 1985.

Krueger, D. A., Caldwell, L. M., She, C. Y., and Alvarez , R. J., II.: Self-consistent Method for Determining Vertical Profiles of Aerosol and Atmospheric Properties Using a High Spectral Resolution Rayleigh-Mie Lidar, J. Atmos. Ocean. Tech., 10(4), 533-545, https://doi.org/10.1175/1520-0426(1993)010<0533:SCMFDV>2.0.CO;2, 1993.

Mamali, D., Marinou, E., Sciare, J., Pikridas, M., Kokkalis, P., Kottas, M., Binietoglou, I., Tsekeri, A., Keleshis, C., Engelmann, R., Baars, H., Ansmann, A., Amiridis, V., Russchenberg, H., and Biskos, G.: Vertical profiles of aerosol mass concentration derived by unmanned airborne in situ and remote sensing instruments during dust events, Atmos. Meas. Tech., 11, 2897–2910, https://doi.org/10.5194/amt-11-2897-2018, 2018.

Mamouri, R. E., Ansmann, A., Nisantzi, A., Kokkalis, P., Schwarz, A., and Hadjimitsis, D. (2013), Low Arabian dust extinction-to-backscatter ratio, Geophys. Res. Lett., 40, 4762-4766, https://doi.org/10.1002/grl.50898, 2013.

Mamouri, R. E. and Ansmann, A.: Fine and coarse dust separation with polarization lidar, Atmos. Meas. Tech., 7, 3717–3735, https://doi.org/10.5194/amt-7-3717-2014, 2014.

Mamouri, R.-E., Ansmann, A., Nisantzi, A., Solomos, S., Kallos, G., and Hadjimitsis, D. G.: Extreme dust storm over the eastern Mediterranean in September 2015: satellite, lidar, and surface observations in the Cyprus region, Atmos. Chem. Phys., 16, 13711–13724, https://doi.org/10.5194/acp-16-13711-2016, 2016

Mamouri, R.-E. and Ansmann, A.: Potential of polarization lidar to provide profiles of CCN- and INP-relevant aerosol parameters, Atmos. Chem. Phys., 16, 5905–5931, https://doi.org/10.5194/acp-16-5905-2016, 2016

Marenco, F., and R. J. Hogan: Determining the contribution of volcanic ash and boundary layer aerosol in backscatter lidar returns: A three-component atmosphere approach, J. Geophys. Res., 116, D00U06, https://doi.org/10.1029/2010JD01F5415, 2011.

Marinou, E., Amiridis, V., Paschou, P., Tsikoudi, I., Tsekeri, A., Daskalopoulou, V., Baars, H., Floutsi, A., Kouklaki, D., Pirloaga, R., Marenco, F., Kazoudi, M., O Connor, E., Pfitzenmaier, L., Zenk, C., Ryder, C., Von Bismarck, J., and Fehr, T. and the ASKOS team: ASKOS Campaign 2021/2022: Overview of measurements and applications, EGU General Assembly 2023, Vienna, Austria, 24–28 Apr 2023, EGU23-16530, https://doi.org/10.5194/egusphere-egu23-16530, 2023.

Nisantzi, A., Mamouri, R. E., Ansmann, A., and Hadjimitsis, D.: Injection of mineral dust into the free troposphere during fire events observed with polarization lidar at Limassol, Cyprus, Atmos. Chem. Phys., 14, 12155–12165, https://doi.org/10.5194/acp-14-12155-2014, 2014.

Nisantzi, A., Mamouri, R. E., Ansmann, A., Schuster, G. L., and Hadjimitsis, D. G.: Middle East versus Saharan dust extinction-to-backscatter ratios, Atmos. Chem. Phys., 15, 7071–7084, https://doi.org/10.5194/acp-15-7071-2015, 2015.

Osborne, M. J., de Leeuw, J., Witham, C., Schmidt, A., Beckett, F., Kristiansen, N., Buxmann, J., Saint, C., Welton, E. J., Fochesatto, J., Gomes, A. R., Bundke, U., Petzold, A., Marenco, F., and Haywood, J.: The 2019 Raikoke volcanic eruption – Part 2: Particle-phase dispersion and concurrent wildfire smoke emissions, Atmos. Chem. Phys., 22, 2975–2997, https://doi.org/10.5194/acp-22-2975-2022, 2022.

Osborne, M. J.: Developing Resilience to Icelandic Volcanic Eruptions, , PhD thesis, University of Exeter, Exeter, http://hdl.handle.net/10871/129640, 2022.

Paschou, P., Siomos, N., Tsekeri, A., Louridas, A., Georgoussis, G., Freudenthaler, V., Binietoglou, I., Tsaknakis, G., Tavernarakis, A., Evangelatos, C., von Bismarck, J., Kanitz, T., Meleti, C., Marinou, E., and Amiridis, V.: The eVe reference polarization lidar system for the calibration and validation of the Aeolus L2A product, Atmos. Meas. Tech., 15, 2299–2323, https://doi.org/10.5194/amt-15-2299-2022, 2022

Reagan, J. A., Spinhirne, J. D., Byrne, D. M., Thomson, D. W., Pena, R. G. D., and Mamane, Y. : Atmospheric Particulate Properties Inferred from Lidar and Solar Radiometer Observations Compared with Simultaneous In Situ Aircraft Measurements: A Case Study, J. Appl. Meteorol. Climatol., 16(9), 911–928, https://doi.org/10.1175/1520-0450(1977)016<0911:APPIFL>2.0.CO;2, 1977.

Sassen, K., Zhu, J., Webley, P., Dean, K. and Cobb, P.: Volcanic ash plume identification using polarization lidar: Augustine eruption, Alaska. Geophys. Res. Lett., 34. L08803, https://doi.org/10.1029/2006GL027237, 2007.

Seifert, P., Ansmann, A., Mattis, I., Wandinger, U., Tesche, M., Engelmann, R., Müller, D., Pérez, C., and Haustein, K.: Saharan dust and heterogeneous ice formation: Eleven years of cloud observations at a central European EARLINET site, J. Geophys. Res., 115, D20201, https://doi.org/10.1029/2009JD013222, 2010.

Senior, C. A., and J. F. B. Mitchell: Carbon Dioxide and Climate. The Impact of Cloud Parameterization, Journal of Climate 6, 3 (1993): 393-418, https://doi.org/10.1175/1520-0442(1993)006<0393:CDACTI>2.0.CO;2, 1993.

Stein, A. F., R. R. Draxler, G. D. Rolph, B. J. B. Stunder, M. D. Cohen, and F. Ngan : NOAA's HYSPLIT Atmospheric Transport and Dispersion Modeling System". Bulletin of the American Meteorological Society 96.12 (2015) 2059-2077. https://doi.org/10.1175/BAMS-D-14-00110.1, 2015.

Tesche, M., Ansmann, A., Müller, D., Althausen, D., Engelmann, R., Freudenthaler, V., and Groß, S.: Vertically resolved separation of dust and smoke over Cape Verde using multiwavelength Raman and polarization lidars during Saharan Mineral Dust Experiment 2008, J. Geophys. Res., 114, D13202, https://doi.org/10.1029/2009JD011862, 2009.

Tesche, M., Groß, S., Ansmann, A., Müller, D., Althausen, D., Freudenthaler, V., and Esselborn, M.: Profiling of Saharan dust and biomass-burning smoke with multiwavelength polarization Raman lidar at Cape Verde, Tellus B, 63, 649–676, https://doi.org/10.1111/j.1600-0889.2011.00548.x, 2011.

Toon, O. B., Tabazadeh, A., Browell, E. V., and Jordan, J.: Analysis of lidar observations of Arctic polar stratospheric clouds during January 1989, J. Geophys. Res., 105(D16), 20589– 20615, https://doi.org/10.1029/2000JD900144, 2000.

Van de Hulst, H.C.: Light Scattering by Small Particles. John Wiley and Sons, New York; Chapman and Hall, London, https://doi.org/10.1063/1.3060205, 1957.

Wandinger, U., Freudenthaler, V., Baars, H., Amodeo, A., Engelmann, R., Mattis, I., Groß, S., Pappalardo, G., Giunta, A., D'Amico, G.,
675   Chaikovsky, A., Osipenko, F., Slesar, A., Nicolae, D., Belegante, L., Talianu, C., Serikov, I., Linné, H., Jansen, F., Apituley, A., Wilson, K.
M., de Graaf, M., Trickl, T., Giehl, H., Adam, M., Comerón, A., Muñoz-Porcar, C., Rocadenbosch, F., Sicard, M., Tomás, S., Lange, D.,
Kumar, D., Pujadas, M., Molero, F., Fernández, A. J., Alados-Arboledas, L., Bravo-Aranda, J. A., Navas-Guzmán, F., Guerrero-Rascado,
J. L., Granados-Muñoz, M. J., Preißler, J., Wagner, F., Gausa, M., Grigorov, I., Stoyanov, D., Iarlori, M., Rizi, V., Spinelli, N., Boselli, A.,
Wang, X., Lo Feudo, T., Perrone, M. R., De Tomasi, F., and Burlizzi, P.: EARLINET instrument intercomparison campaigns: overview on
680   strategy and results, Atmos. Meas. Tech., 9, 1001–1023, https://doi.org/10.5194/amt-9-1001-2016, 2016.

Yin, Z. and Baars, H.: PollyNET/Pollynet Processing Chain: Version 2.1, Zenodo, https://doi.org/10.5281/zenodo.4694451, 2021.